11-20-2000

Hubble Space Telescope Imaging Spectrograph Observations of the Hot White Dwarf in the Close Binary Feige 24

Stephane Vennes
Australian National University

Elisha F. Polomski
University of Florida

Thierry Lanz
University of Maryland

John R. Thorstensen
Dartmouth College

Recommended Citation

Vennes, Stephane; Polomski, Elisha F.; Lanz, Thierry; and Thorstensen, John R., "Hubble Space Telescope Imaging Spectrograph Observations of the Hot White Dwarf in the Close Binary Feige 24" (2000). *Open Dartmouth: Faculty Open Access Articles*. 2273.
https://digitalcommons.dartmouth.edu/facoa/2273

THE ASTROPHYSICAL JOURNAL, 544:423–436, 2000 November 20

HUBBLE SPACE TELESCOPE IMAGING SPECTROGRAPH OBSERVATIONS OF THE HOT WHITE DWARF IN THE CLOSE BINARY FEIGE 24

STÉPHANE VENNES,[1] ELISHA F. POLOMSKI,[2] THIERRY LANZ,[3] JOHN R. THORSTENSEN,[4]
PIERRE CHAYER,[5] AND TED R. GULL[6]

Received 2000 April 11; accepted 2000 June 28

ABSTRACT

We obtained and analyzed two *Hubble Space Telescope* Imaging Spectrograph spectra of the white dwarf in the DA plus dMe binary Feige 24. The spectra, obtained at orbital quadratures, provide new estimates of the white dwarf motion and gravitational redshift resulting in revised white dwarf parameters. An analysis of interstellar absorption lines reveals the presence of two clouds (+3.1 km s^{-1}, +17.6 km s^{-1}) in the line of sight toward Feige 24; one of these clouds (+17.6 km s^{-1}) is identified with the "local cloud." A study of the Lyα H I and D I interstellar medium lines shows that the deuterium-to-hydrogen abundance ratio ($D/H = 1.3 \times 10^{-5}$) is consistent with other measurements supporting a relative constancy of this ratio throughout the local interstellar medium. The total hydrogen column density measured with Lyα ($\log n_H = 2.95 \times 10^{18}$ cm^{-2}) is in agreement with EUV Lyman continuum flux measurements. Finally, we present a complete abundance pattern for the white dwarf, demonstrating the predominance of iron and nickel over lighter elements. Residual ionization imbalance in the case of several elements, most notably in the case of O IV/O V, which cannot be explained by temperature or surface gravity variations, may indicate the presence of other atmospheric constituents, inhomogeneous stratification of oxygen in the photosphere, and/or remaining inaccuracies in the treatment of model atoms. The abundance patterns in Feige 24 and in the hot DA white dwarf G191-B2B are remarkably similar, indicating that the same processes are operating equally in both stars.

Subject headings: ISM: abundances — stars: abundances — stars: individual (Feige 24) — ultraviolet: stars — white dwarfs

1. INTRODUCTION

The hot white dwarf in the close binary Feige 24 (Feige 1958; PHL 1376: Haro & Luyten 1962; EG 20: Eggen & Greenstein 1965; RE J0235+034: Pye et al. 1995; EUVE J0235+037: Bowyer et al. 1996) is a bright far-ultraviolet (FUV) and extreme ultraviolet (EUV) source. The white dwarf was first cataloged by Feige (1958) in a search for faint blue stars on the National Geographic–Palomar Sky Survey. Feige noted that star 24 shows an ultraviolet excess. Eggen & Greenstein (1965) later noted "relatively sharp and weak H emission lines … and also Ca II emission" and suggested that the object is "perhaps an old nova," although Greenstein & Eggen (1966) refer to Feige 24 as possibly a prenova, "resembling WZ Sagittae," but with a wider orbital separation. Oke's (1974) multichannel spectroscopy clearly shows a red dwarf companion, and Liebert & Margon (1977) noted spectral variability which could be explained by flare activity or, more likely, "caused by binary phase-dependent effects of ionizing radiation from the white dwarf on the red component."

Indeed, Feige 24 was only the second extrasolar EUV source discovered (Margon et al. 1976), and both optical (Shipman 1972) and OAO 2 ultraviolet photometry (Holm 1976) indicate a high temperature ($T_{\rm eff} \geq 50{,}000$ K). Based on their broadband EUV photometric data, Margon et al. (1976) deduced the presence of soft X-ray opacities in the white dwarf atmosphere. The effect of EUV/soft X-ray opacities was also evident in the *EXOSAT* LETG spectrum of the white dwarf (Paerels et al. 1986), which Vennes et al. (1989) successfully interpreted with a hot model atmosphere ($T_{\rm eff} = 55{,}000$, $\log g = 7.23$) contaminated by a host of trace heavy elements. The original model has recently been updated by Wolff et al. (1998) who included iron cross sections from the Opacity Project (see Pradhan 1996) in their analysis of the *Extreme Ultraviolet Explorer* (*EUVE*) spectrum of Feige 24.

Thorstensen et al. (1978) obtained the first set of orbital elements for this 4.23 day system and developed an EUV illumination and reprocessing model to explain the regular variations of the emission spectrum: maximum equivalent width lags the maximum radial velocity by one quarter of the orbital period, as predicted by the model. Using a set of *IUE* high-dispersion spectra, Vennes et al. (1991) also measured the orbit of the white dwarf, and using KPNO echelle and additional *IUE* high-dispersion spectra Vennes & Thorstensen (1994, hereafter VT94) established the long-term ephemeris and determined the orbital elements of the system.

Located at a distance of ∼70 pc toward a low-density line of sight of the interstellar medium (ISM), Feige 24 is also an excellent FUV background source for studies of absorption lines in the local ISM (LISM). Dupree & Raymond's (1982) study of Feige 24 with the *International Ultraviolet Explorer* (*IUE*) uncovered N I, O I, and Si II resonance lines in the ISM as well as two well-separated components of the C IV λ1549.1 doublet, one possibly cir-

---

[1] Postal address: Department of Mathematics, Australian National University, Canberra ACT 0200, Australia.

[2] Department of Astronomy, University of Florida, Gainesville, FL 32611.

[3] Department of Astronomy, University of Maryland, College Park, MD 20742.

[4] Department of Physics and Astronomy, Dartmouth College, Hanover, NH 03755.

[5] Bloomberg Center for Physics and Astronomy, Johns Hopkins University, Baltimore, MD 21218.

[6] NASA Goddard Space Flight Center, Code 680, Greenbelt, MD 20771.

cumstellar and the other photospheric. Based on the mean radial velocity of the ISM lines, they found "no evidence that the gas to Feige 24 is connected with the local ISM described by Crutcher (1982)." Dupree & Raymond (1982) also listed photospheric lines of N V and Si IV. From these measurements, Wesemael, Henry, & Shipman (1984, hereafter WHS) determined abundances of C, N, and Si well below solar.

Interest in Feige 24, both from a stellar evolution and from an ISM perspective, has motivated the acquisition of two *Hubble Space Telescope* (*HST*) Imaging Spectrograph (STIS) spectra in 1997 November and 1998 January (§ 2). New model atmospheres required for the interpretation of the ultraviolet spectroscopy are described in § 3, followed by a discussion of the orbital parameters (§ 4), the properties of the ISM (§ 5), and the chemical composition of the white dwarf atmosphere (§ 6). We summarize in § 7.

2. OBSERVATIONS

2.1. *Complete Spectral Energy Distribution*

Figure 1 shows the complete spectral energy distribution of the binary Feige 24 including *EUVE* spectroscopy from Dupuis et al. (1995), *IUE* spectroscopy (LWR03325, SWP03740), and Oke's (1974) multichannel spectrometer (MCSP) data which show the sum of the white dwarf and cool red dwarf. MCSP fluxes were given in terms of AB magnitudes. An EUV spectrum of Feige 24, deattenuated for interstellar absorption using H I/He I column densities from Dupuis et al 1995), is compared to a pure hydrogen model at $T_{\rm eff} = 64{,}000$ K. A dramatic disparity between model and observation is seen at shorter wavelengths ($\lambda \leq 250$ Å) due to the presence of heavy-element opacities. A lower effective temperature of 56,000 K was also measured by Dupuis et al. based on high-metallicity models rather than pure hydrogen models, in agreement with an analysis of the Balmer line series ($T_{\rm eff} = 56{,}370$, $\log g = 7.36$) using high-metallicity models (Barstow, Hubeny, & Holberg 1998). In the following, we adopt an effective temperature in the range 55,000–57,000 K and a low surface gravity ($\log g = 7.3$–7.5) consistent with current orbital and spectroscopic studies (see § 4.2).

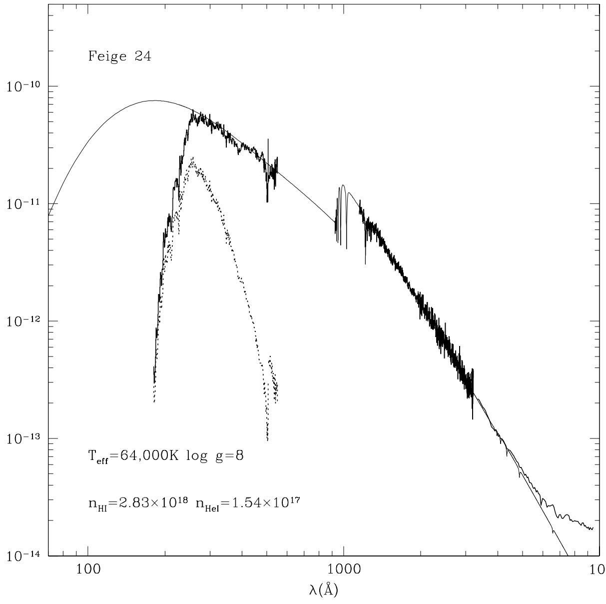

FIG. 1.—Complete spectral energy distribution of Feige 24 based on *EUVE* spectroscopy (Dupuis et al. 1995), *IUE* low-dispersion spectroscopy (LWR03325, SWP03740), and multichannel spectrophotometry (Oke 1974). The EUV fluxes are shown corrected for H I and He I attenuation in the ISM (*full line*) and uncorrected (*dotted line*). The corrected fluxes are compared to a pure hydrogen model at 64,000 K (*full line*) which fails to account for short-wavelength opacities. The M dwarf companion dominates the distribution at 1 μm.

2.2. *HST STIS*

Our observations were conducted with the *HST* STIS FUV Multianode Microchannel Array (MAMA) echelle spectrograph (Table 1). In order to maximize the signal-to-noise ratio, we utilized a 0."2 × 0."2 aperture in conjunction with the E140M ($\lambda = 1142$–1730 Å) grating. Observations were conducted on 1997 November 29 (binary phase 0.73–0.75) and 1998 January 4 (binary phase 0.23–0.25) with total exposure times of 2016 and 2160 s, respectively. The summed spectrum, in either the stellar or interstellar rest frame, has a signal-to-noise ratio of ~ 50.

The standard STSDAS STIS calibration pipeline failed for our observations. Thus, we ran the STSDAS CALSTIS[7] pipeline under IRAF and in addition recalibrated the wavelength solution using GO WAVECALS which we had obtained immediately following the science exposures. Wavelength calibration was obtained utilizing the standard Pt-Cr/Ne line comparison lamp. The velocity scale is accurate to within 1.4 km s^{-1} based upon the reproducibility of interstellar line profiles.

The STIS echelle spectrograph suffers from scattered light contamination in the ultraviolet. This contamination will result in oversubtraction of the background. At Lyα we estimate an 11% contribution from scattered light. T. R. Gull corrected our data set for this problem using an interactive data language (IDL) procedure developed by Bowers et al. (2000, in preparation) and the STIS Instrument Definition Team. The routine ECHELLE SCAT uses the original net flux from CALSTIS as a first guess of the flux distribution. A first iteration adopts the current flux distribution and constructs a model light image using reference models

TABLE 1

STIS OBSERVATIONS LOG (FUV-MAMA)

Date (UT)	Root Name	HJD (2,450,000+)	Orbital Φ[a]	Grating	λ Range (Å)	$t_{\rm exp}$ (s)	Aperture (arcsec)
1997 Nov 29......	O4G702010	781.95742	0.739	E140M	~1142–1730	2016	0.2 × 0.2
1998 Jan 04.......	O4G701010	817.91598	0.237	E140M	~1142–1730	2160	0.2 × 0.2

[a] From VT94's ephemeris.

---

[7] See D. C. Lindler's CALSTIS Reference Guide, April 30, 1999 (v6.4) at http://hires.gsfc.nasa.gov/stis/software/doc_manuals.html.

for the echelle scatter function, the telescope point-spread function, the detector halo and grating isotropic scattering, the cross-disperser scatter function, and detector ghosts. A new net spectrum is extracted using the same parameters as specified in the original call to CALSTIS. The difference in net spectrum is used to correct the flux distribution, and the full procedure is iterated a second time. On the third and final iteration, the model light scattered image is subtracted away from the original flat-fielded count rate image. The final spectrum is extracted and flux calibrated using the same parameters as in the original call to CALSTIS. Some scattered light residuals are still apparent in the core of Lyα but absent from the saturated cores of O I and C II lines.

Because we adopted the $0''.2 \times 0''.2$ aperture, the limiting resolving power of our observations is dependent upon the point-spread function of *HST*. The average of measurements of the FWHM of the spectrum perpendicular to the echelle dispersion is, after correcting for anamorphic distortions, 2.5 pixels corresponding to a "measured resolving power" of $\sim$36,600.

2.3. *IUE*

We retrieved 14 short-wavelength prime camera (SWP) images from the *IUE* archive through the Multimission Archive at STScI. We extracted the spectra by using the NEWSIPS data processing system. All spectra were obtained in the high-dispersion mode with the large aperture, except for the SWP25163 spectrum where the small aperture was used. For abundance work, we built a summed spectrum by shifting the wavelength scale of each spectrum using VT94's ephemeris and by restoring the photospheric line wavelengths back to rest values. We resampled and then co-added the spectra using the exposure time for weighting. The resulting co-added spectrum corresponds to $\sim$64 hr of integration and has a signal-to-noise ratio of 25.

Ten of the above spectra which were originally processed with IUESIPS were also obtained from the archives to compare wavelength solutions and measured abundances with NEWSIPS. The wavelength scale of the IUESIPS spectra was corrected for drift using the *IUE* RDAF procedure DCCOR.

3. MODEL ATMOSPHERES

3.1. *LTE*

Vennes, Pradhan, & Thejll (1995, private communication) computed a grid of model atmospheres including heavy-element opacities. Tables of C, N, O, and Fe opacities in the log n_e versus log T plane were computed using Opacity Project cross sections (multiplet bound-bound, bound-free, and free-free) assuming local thermodynamic equilibrium (LTE). The total monochromatic opacity, with relative abundance listed in Table 2 under LTE/OP, was used as an input to the model atmosphere code ATLAS9. Dupuis et al. (1995) adopted these LTE models in their analysis of the EUV Lyman continuum of Feige 24. Detailed line profiles of C, N, O, Si, S, Fe, and Ni with variable abundance were computed around a fixed model structure.

3.2. *NLTE*

A series of models in non–local thermodynamic equilibrium (NLTE) were computed by T. Lanz using the model atmosphere code TLUSTY (Hubeny 1988; Hubeny & Lanz 1995). The models used in the present investigation correspond to a modified fully blanketed "FB" generation of models described in Lanz, Hubeny, & Heap (1997), as opposed to the limited blanketed "LB" generation used by Lanz & Hubeny (1995). The FB models include 118 iron "superlevels" totaling 30,432 individual levels for the Fe IV/Fe V/Fe VI/Fe VII ions, while the LB models included 52 iron superlevels totaling 550 detailed levels for the same ions. The difference between the two generations of models amounts to the inclusion of "predicted" iron energy levels as well as the "observed" levels. The present models also include equally sophisticated treatment of the nickel ions Ni IV/Ni V/Ni VI/Ni VII. The far greater completeness of the latest generation of models should lead to better insights into the iron ionization balance. The content of the light-ion list of atomic energy levels of Lanz et al.'s (1997) FB models was modified in the following way.

The models include the following light-element ions with the number of levels between parentheses: H I (9 levels), He I (24 levels), He II (14 levels), C II (22 levels), C III (23 levels), C IV (24 levels), C V (ground state only), N II (26 levels), N III (31 levels), N IV (23 levels), N V (12 levels), N VI (ground state only), O II (16 levels), O III (29 levels), O IV (38 levels), O V (40 levels), O VI (20 levels), O VII (ground state only), Si III (30 levels), Si IV (22 levels), and Si V (ground state only).

The models also include for the first time a sulfur model atom: S III (10 levels), S IV (14 levels), S V (12 levels), S VI (9 levels), and S VII (ground state only).

The abundances are listed in Table 2 under the labels TLUSTY. The NLTE models are used to predict an accu-

TABLE 2

Model Atmospheres

			log X/H							
Model	$T_{\rm eff}$ (10^3 K)	log g (cgs)	He	C	N	O	Si	S	Fe	Ni
LTE/OP	56	7.5	...	−6.4	−5.3	−6.0	...	...	−5.0	...
TLUSTY......	55	7.3	−5.0	−7.0	−7.0	−5.8	−6.0	...	−5.15	−5.5
TLUSTY......	55	7.5	−5.0	−7.0	−7.0	−5.8	−6.0	...	−5.15	−5.5
TLUSTY......	57	7.5	−5.0	−7.0	−7.0	−5.8	−6.0	...	−5.15	−5.5
TLUSTY......	55	7.5	−5.0	−7.1	−7.1	−6.5	−6.5	−7.0	−5.7	−6.0
TLUSTY......	55	7.5	−5.0	−6.7	−6.4	−5.6	−5.8	−6.0	−5.0	−5.5
TLUSTY......	57	7.5	−5.0	−7.1	−7.1	−6.5	−6.5	−7.0	−5.7	−6.0
TLUSTY......	57	7.5	−5.0	−6.7	−6.4	−5.6	−5.8	−6.0	−5.0	−5.5
TLUSTY......	57	7.3	−5.0	−7.1	−7.1	−6.5	−6.5	−7.0	−5.7	−6.0
TLUSTY......	57	7.3	−5.0	−6.7	−6.4	−5.6	−5.8	−6.0	−5.0	−5.5

rate Lyα photospheric line profile allowing extraction of a pure interstellar deuterium/hydrogen line profile. Narrow heavy-element lines are also used for radial velocity measurements of the white dwarf.

4. ORBITAL PARAMETERS

4.1. *Revised Systemic* (γ) *and White Dwarf Orbital Velocity* ($K_{\rm WD}$)

Heliocentric radial velocities at both epochs are obtained with cross-correlations of the STIS spectra with respect to the NLTE spectral synthesis. The position of the cross-correlation peak is insensitive to actual model abundances, but the significance of the peak may be affected by abundances through the line strengths. The model ($T_{\rm eff}$, log g, log [C, N, O, Si, Fe, Ni]/H) = (55,000, 7.3, −7.0, −7.0, −5.8, −6.0, −5.15, −5.5) was adopted. Table 3 lists the velocities extracted from five wavelength intervals. The mean values at both orbital phases are 9.4 ± 1.0 km s^{-1} larger than predicted by VT94's orbital elements suggesting that the STIS-based velocity scale exceeds the IUESIPS-based velocity scale by 9.4 km s^{-1}. The resulting apparent systemic velocity (i.e., augmented by the white dwarf gravitational redshift) may be compared to VT94's measurement (formal errors only):

$$\gamma = 70.2 \pm 1.9 \text{ km s}^{-1} \text{ (IUESIPS)} ,$$

$$\gamma = 79.6 \pm 2.3 \text{ km s}^{-1} \text{ (STIS)} .$$

Table 4 lists, order by order, cross-correlation velocities of the spectrum at $\Phi = 0.237$ relative to the spectrum at $\Phi = 0.739$. Orders with low signal-to-noise ratios or clearly dominated by ISM spectral lines are excluded. An accurate orbital velocity amplitude is extracted from the mean cross-correlated velocity and may be compared to VT94's measurement (formal errors only):

$$K_{\rm WD} = 47.8 \pm 2.8 \text{ km s}^{-1} \text{ (IUESIPS)} ,$$

$$K_{\rm WD} = 49.1 \pm 0.3 \text{ km s}^{-1} \text{ (STIS)} .$$

Taking into account possible systematic errors of 3.0 and 1.4 km s^{-1} for *IUE* (Thompson, Turnrose, & Bohlin 1982) and STIS (§ 2.2), respectively, we conclude that the $K_{\rm WD}$ velocities based on either the IUESIPS or the STIS velocity scale are in excellent agreement but that heliocentric velocities differ by $v_{\rm STIS} - v_{\rm IUESIPS} = 9.4$ km s^{-1}. Adopting VT94's systemic velocity based on the red dwarf orbital motion, we deduce a white dwarf gravitational redshift of $\gamma_g = 18.1 \pm 2.7$ km s^{-1}, which exceeds VT94's estimate by ~9 km s^{-1}. The two velocity scales (*IUE* vs. STIS) clearly disagree, and an examination of ISM line velocities may help elucidate the question.

TABLE 3

Cross-Correlation Velocities: STIS versus Spectral Synthesis

Range (Å)	$v_{\Phi 0.237}$ (km s^{-1})	$v_{\Phi 0.739}$ (km s^{-1})
1230–1330	32.8 ± 0.9	130.5 ± 1.0
1330–1430	31.7 ± 0.4	129.3 ± 0.5
1430–1530	31.1 ± 0.6	128.7 ± 0.4
1530–1630	27.8 ± 1.2	127.8 ± 1.3
1630–1730	29.4 ± 4.3	126.5 ± 3.6
All	30.6 ± 1.8	128.6 ± 1.4
IUE (VT94)......	22.5 ± 3.4	117.8 ± 3.4

TABLE 4

Cross-Correlation Velocities: $\Phi = 0.237$ versus $\Phi = 0.739$

Order	Range (Å)	v (km s^{-1})	Notes/Dominant Features
1–9	...	...	Low S/N
10–11	...	...	C IV circumstellar
12–14	...	...	Featureless
15	1471.3–1486.7	−98.2 ± 1.2	
16	1456.9–1471.9	−97.9 ± 0.8	
17	1442.2–1457.5	−97.6 ± 1.0	
18	1428.3–1442.5	−98.3 ± 0.9	
19	...	...	
20	1401.2–1415.7	−98.2 ± 0.6	Si IV
21	1387.8–1402.1	−98.2 ± 1.1	Si IV
22	1374.7–1388.3	−97.4 ± 1.1	
23	1362.2–1376.6	−97.5 ± 1.2	
24	1349.5–1363.9	−97.3 ± 1.0	
25	1337.3–1351.5	−96.7 ± 1.1	
26	...	...	C II ISM
27	1313.3–1327.3	−97.9 ± 0.7	
28	1302.6–1315.6	−97.7 ± 1.3	
29	...	...	O II ISM
30	1279.1–1292.7	−99.0 ± 2.7	
31	1268.1–1281.5	−97.5 ± 1.1	
32	...	...	Si II ISM
33	1246.5–1259.8	−99.2 ± 1.5	
34	1236.1–1249.2	−98.4 ± 0.9	N V
35	1225.8–1238.7	−101.5 ± 3.1	
36–37	...	...	Lyα wing
38	...	...	Si III + N I ISM
39	...	...	Si II ISM
40–44	...	...	Low S/N
All		−98.0 ± 0.6	

4.2. *Revised White Dwarf Mass and Radius*

Figure 2 shows our most recent version of VT94's mass-radius diagram constrained by our new white dwarf gravitational redshift, Wood's (1995) evolutionary mass-radius relations at $T_{\rm eff} = 56{,}000$ K for carbon interiors with and without hydrogen envelopes ($10^{-4} M_*$), and finally Benedict et al.'s (2000) parallax measurement. Benedict et al. used the *HST* Fine Guidance Sensor 3 (FGS 3) to measure a parallax of $\pi = 14.7 \pm 0.6$ mas. Using the flux ratio based on Holberg, Wesemael, & Basile's (1986) flux decomposition at V ($V_{\rm WD} = 12.56 \pm 0.05$) and our LTE model flux at $T_{\rm eff} = 56{,}000 \pm 1000$ K [$H_V = (7.58 \pm 0.09) \times 10^{-4}$], the parallax measurement translates into a radius of $R_{\rm WD} = 0.0182 \pm 0.0013$ $R_\odot$. From these constraints we conclude that Feige 24 is a white dwarf with a carbon core and the following mass and radius:

$$({\rm C_{WD}}) \quad M = 0.458\text{–}0.516\, M_\odot , \quad R = 0.0169\text{–}0.0195\, R_\odot ,$$

$$({\rm CH_{WD}}) \quad M = 0.532\text{–}0.568\, M_\odot , \quad R = 0.0177\text{–}0.0195\, R_\odot .$$

However, the corresponding surface gravity (log g = 7.5–7.7) is only marginally consistent with the surface gravity measurements of Marsh et al. (1997), 7.53 ± 0.09, and Barstow et al. (1998), 7.36 ± 0.12, and inconsistent with the measurements of Finley, Koester, & Basri (1997), 7.17 ± 0.15, and Vennes et al. (1997), 7.20 ± 0.07. A varying degree of contaminations by Ca II and H I emission lines may explain part of the discrepancy, but in a more general context Napiwotzki, Green, & Saffer (1999) noticed systematic offsets in surface gravity measurements among various investigations. These offsets are largely in excess of 1 σ error

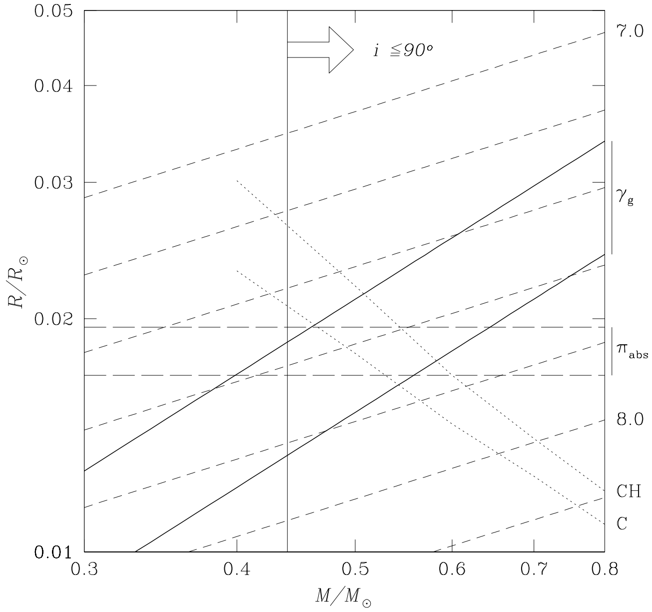

FIG. 2.—New constraints on the mass and radius of Feige 24: *HST* STIS gravitational redshift (γ_g), *HST* FGS 3 parallax (π_{abs}), and Wood's (1995) evolutionary mass-radius relations for carbon interiors with a $10^{-4}M_*$ hydrogen envelope (CH) and without (C). Curves of constant gravity are shown from log $g = 7.0$ to 8.2 with 0.2 dex increment; curves at log $g = 7.0$ and 8.0 are labeled. A minimum mass of 0.44 $M_\odot$ is imposed using Kepler's third law.

bars quoted in the same investigations. The present gravitational redshift and recent parallax measurements clearly support a smaller radius than previously discussed by VT94. A spectroscopic surface gravity measurement based on the FUV Lyman line series may resolve the issue.

5. INTERSTELLAR MEDIUM

5.1. *Hydrogen and Helium Column Densities*

The line of sight toward Feige 24 is characterized by low neutral hydrogen and neutral helium column densities (Dupuis et al. 1995):

$$\log N_{\text{H I}} = 18.47 \pm 0.03 ,$$

$$\log N_{\text{He I}} = 17.20 \pm 0.05 .$$

Assuming a cosmic abundance ratio of $N_{\text{H}}/N_{\text{He}} = 10$, the column densities in this line of sight suggest overionization of helium relative to hydrogen.

5.2. *Two-Component Interstellar Medium*

5.2.1. *Removal of Photospheric Lines*

A simple but effective technique was used to remove the photospheric line spectrum from the co-added STIS spectrum. (1) We used the accurate cross-correlation velocity $\Delta v = -98.0$ km s^{-1} to align the photospheric spectrum at $\Phi = 0.237$ with the spectrum at $\Phi = 0.739$, and (2) we defined the ratio of the two spectra $S = S_{\Phi 0.237}/S_{\Phi 0.739}$. (3) The spectrum S was then restored to the original velocity scale at $\Phi = 0.237$ and labeled S', and (4) a cleaned ISM spectrum is obtained by averaging S and S': $S_{\text{ISM}} = (S + S')/2$. The procedure could not be applied to the N I λ1199.9 triplet because of the close wavelength separation between the lines, and instead the ISM spectrum was built by summing $S_{\text{ISM}} = (S_{\Phi 0.237} + S_{\Phi 0.739})/2$. The two separate spectra of the N I triplet show identical line shapes and no apparent contamination from photospheric lines.

5.2.2. *Two Components*

A search for steady velocity spectral lines presumably associated with the interstellar medium or hypothetical circumstellar shell about Feige 24 results in detections of C II, N I, O I, Si II/Si III, and S II lines (Table 5) as well as C IV and Si IV lines. The equivalent widths and wavelength centroids were measured with IRAF's SPLOT Gaussian fit "k" function for single components or deblended with IRAF's SPLOT double Gaussian "d" function for two components. The error is estimated at 5% with minimum error of 1 mÅ. The velocities (in parenthesis) were measured from the laboratory wavelengths (λ_{lab}). Most lines show two velocity components suggesting the presence of at least two intercepting clouds. Figure 3 shows summed data: a first component (I) which we attribute to the local ISM is found at $+17.6$ km s^{-1} and a second component (II) at $+3.1$ km s^{-1}. Crutcher (1982) and Lallement et al. (1995) determined the vector describing the motion of the local interstellar cloud (LIC) and predicted a projected motion of $V_{\text{LIC}} = +17.4$ and $+20.5$ km s^{-1} in the line of sight toward Feige 24 ($l = 165.97, b = -50.27$), respectively.

5.2.3. *Velocity Scale of the ISM*

The ISM velocity toward Feige 24 measured with *IUE* by Dupree & Raymond (1982) is $v_{\text{ISM}} = -3.3 \pm 5$ km s^{-1}, which Holberg, Barstow, & Sion (1998) reestimated at $v_{\text{ISM}} = -3.2 \pm 1$ km s^{-1} based on NEWSIPS spectra (including an ad hoc correction to the NEWSIPS velocity scale of $+8.8$ km s^{-1}). Our own IUESIPS measurements based on 10 spectra yield $v_{\text{ISM}} = -0.6 \pm 4.3$ km s^{-1}. Note that in the case of Feige 24 the difference between IUESIPS and NEWSIPS stellar velocities, based on 14 spectra, is $v_{\text{IUESIPS}} - v_{\text{NEWSIPS}} = +4.3 \pm 4.8$. Smoothing the STIS spectrum to *IUE*'s spectral resolution ($R \sim 10{,}000$) results in the blending of both ISM components and in a mean ISM velocity scale $v_{\text{ISM,STIS}} = +7.4 \pm 1.7$ km s^{-1}. We may conclude again (see § 4) that the *IUE* velocity scale is ∼8.0 km s^{-1} short of the STIS velocity scale.

On the other hand, if we assume that the *IUE* velocity scale is correct and adjust the *STIS* velocity scale to match *IUE*, we find corrected velocities for the two ISM components of $v_{\text{ISM,I}} = +9.3$ km s^{-1} and $v_{\text{ISM,II}} = -5.5$ km s^{-1}. The local cloud which is expected at 17–20 km s^{-1} would be absent from the line of sight, which is unlikely considering its detection in several other lines of sight. The *STIS* velocity scale appears to be the correct one, but our column density measurements, described below, may help determine the relative importance of clouds I and II and confirm the likelihood of an identification of the LIC with cloud I using the *STIS* velocity scale.

5.3. *Deuterium-to-Hydrogen Abundance Ratio*

Figure 4 (*right panel*) shows H I/D I Lyα absorption in the interstellar medium. Before co-addition, the two STIS spectra are normalized to unity using the white dwarf model flux with the velocity scale adjusted to the photospheric velocity of each spectrum. The summed spectrum is then fitted with Voigt profiles assuming two separate ISM components ($v = 3.1$ and 17.6 km s^{-1}). The D I/H I abundance ratio is assumed identical in both clouds. Figure 4 (*left*

TABLE 5

TWO-COMPONENT ISM: VELOCITIES AND EQUIVALENT WIDTHS

ION	$\lambda_{\rm lab}$ (Å)	f_{ij}[a]	$\lambda_{\rm obs}$ (v)[b] I	$\lambda_{\rm obs}$ (v)[b] II	EW (mÅ) I	EW (mÅ) II
C II	1334.5323	0.1278	1334.613 (+18.1)	1334.542 (+2.2)	70.1	71.6
	1335.7032[c]	0.1277	...	1335.725 (+4.9)	...	16.7
N I	1199.5496	0.1328	1199.618 (+17.1)	1199.560 (+2.6)	30.7	39.4
	1200.2233	0.0885	1200.291 (+16.9)	1200.235 (+2.9)	21.3	29.3
	1200.7098	0.0442	1200.779 (+17.3)	1200.717 (+1.8)	13.8	17.6
O I	1302.1685	0.0489	1302.243 (+17.2)	1302.180 (+2.6)	58.5	58.9
Si II	1190.4158	0.291	1190.488 (+18.2)	1190.426 (+2.6)	17.2	31.9
	1193.2897	0.580	1193.357 (+16.9)	1193.298 (+3.1)	30.2	44.4
	1260.4221	1.147	1260.491 (+16.4)	1260.432 (+2.4)	43.3	50.8
	1304.3702	0.101	1304.453 (+19.0)	1304.384 (+3.2)	7.2	25.8
	1526.7066	0.116	1526.805 (+19.3)	1526.722 (+3.0)	12.4	36.3
Si III......	1206.500	1.669	...	1206.520 (+5.0)	...	33.5
S II	1250.584	0.0055	...	1250.603 (+4.5)	...	3.4
	1253.811	0.0109	...	1253.825 (+3.3)	...	7.1
	1259.519	0.0162	...	1259.532 (+3.1)	...	10.1

[a] f_{ij} from Morton 1991, except Si II from Luo et al. 1988.

[b] Units in Å (km s^{-1}).

[c] f_{ij} and λ for doublet $\lambda\lambda$1335.6627–1335.7077.

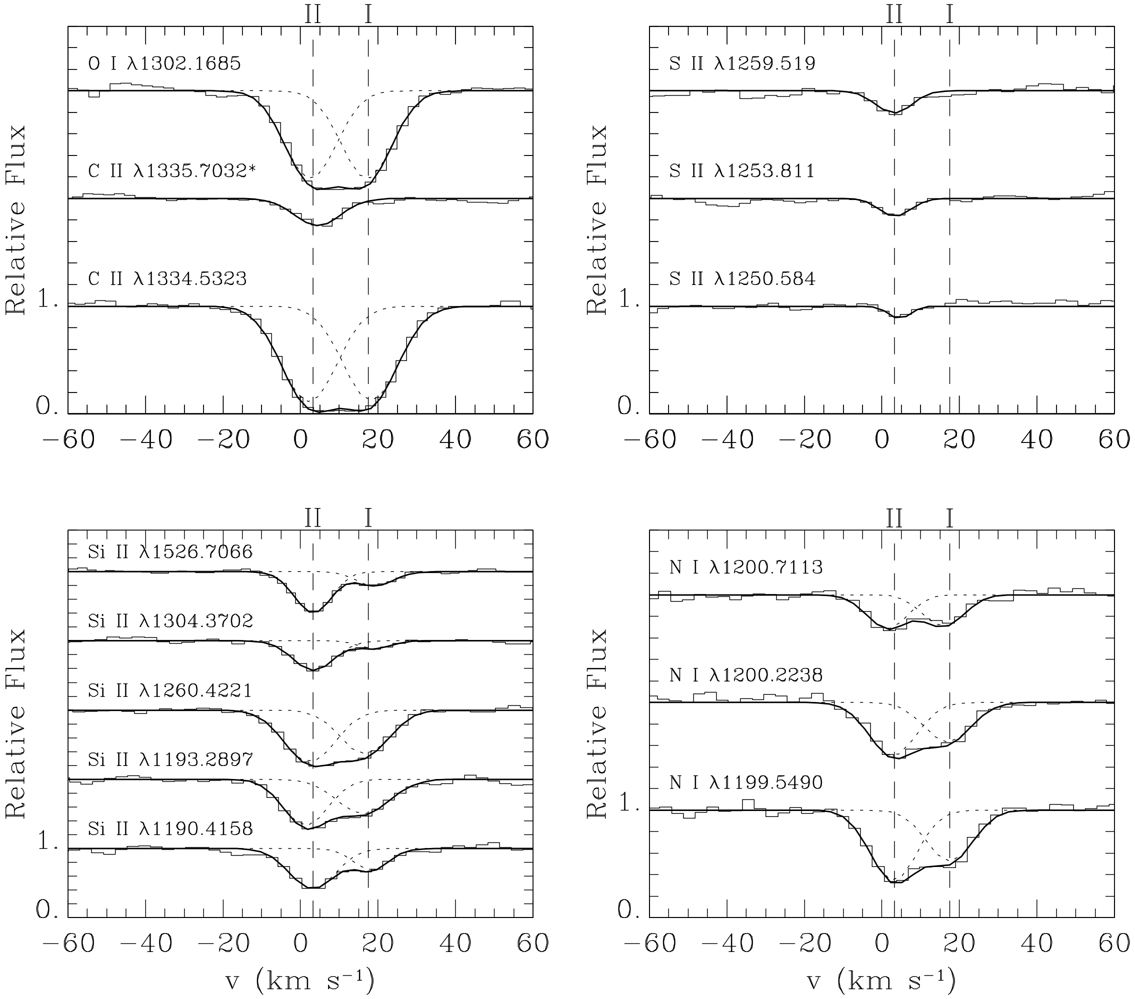

FIG. 3.—Decomposition of ISM lines into two separate velocity components at +3.1 and +17.6 km s^{-1}. All lines, excluding those from S II and the excited line of C II λ1335.7032, show the two components.

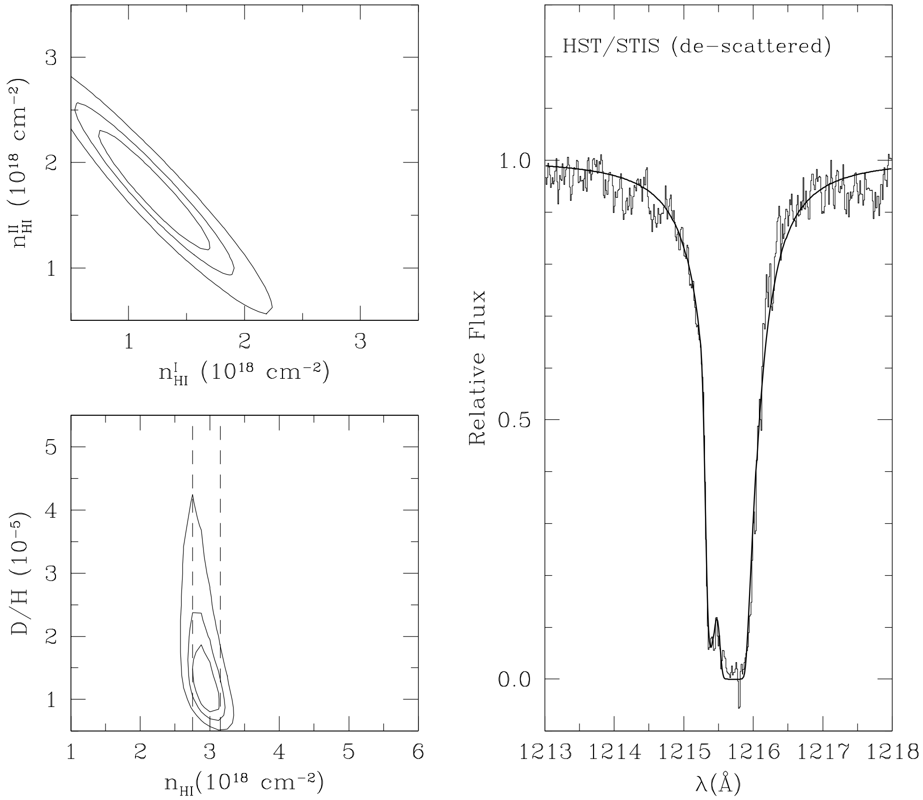

FIG. 4.—Analysis of D I and H I absorption in the local ISM (*left panels*) indicating a total H I column density in the line of sight of 2.95×10^{18} cm^{-2} and a D I/H I ratio of 1.3×10^{-5}, and the best Lyα profile fit (*right panel*). The fit assumes the presence of two distinct velocity components (§ 5.2), and the photospheric line absorption has been removed using a line-blanketed NLTE model at $T_{\rm eff} = 57{,}000$ K and $\log g = 7.5$.

panels) shows results of the three-parameter χ^2 analysis—H I column density of cloud I, H I column density of cloud II, and the total deuterium-to-hydrogen abundance ratio—in the D/H versus total H I column density plane and the H I component II versus component I plane. The best line profile fit indicates $\log N_{\rm H\,I}({\rm I}) = 18.08$, $\log N_{\rm H\,I}({\rm II}) = 18.24$, and D/H $= 1.3 \times 10^{-5}$.

The measured D/H ratio toward Feige 24 can be compared to other measurements toward nearby objects, most notably D/H $= 1.6 \times 10^{-5}$ toward Capella (Linsky et al. 1995), D/H $= 1.6 \times 10^{-5}$ in the LIC toward Sirius A/B (Hébrard et al. 1999), and D/H $= 1.6 \times 10^{-5}$ in the LIC toward the white dwarf G191-B2B (Sahu et al. 1999). The deuterium abundance in the ISM appears nearly constant within ~70 pc; Linsky & Wood (1998) obtained an average of D/H $= (1.6 \pm 0.2) \times 10^{-5}$ in 11 lines of sight—but uniformity may extend to even larger distances such as toward BD +39°3226 ($d = 270$ pc) for which ORFEUS-II measurements yield D/H $= (1.2 \pm 0.3) \times 10^{-5}$ (Bluhm et al. 1999). Possible variations of the D/H ratio in the LISM have been suggested, in particular, within a second cloud discovered toward Sirius A/B (Hébrard et al. 1999).

Because the two deuterium components are not separable in our spectrum, we cannot examine possible D/H variations between cloud I and cloud II; however, the mean value in this line of sight does not indicate significant variations.

5.4. C II *Column Density and the ISM Electron Density*

The strong C II λ1334.5323 line is a blend of two almost identical ISM components and emerges from the C II ground state level ($E_j = 0$). A weaker C II λ1335.6627–1335.7077 line, emerging from the excited level at $E_k = 63.42$ cm^{-1}, is identified with the ISM component II only.

Table 6 presents the results of the curve-of-growth analysis for the ground-state line using C II line data from Morton (1991). It is not possible to constrain both the column density (N) and the velocity dispersion (b) with a single line, and we determined the column densities allowing b to vary between 3.5 and 10.0 km s^{-1} in cloud II and between 4.0 and 10.0 km s^{-1} in cloud I. Adopting the hydrogen column densities within clouds I and II from § 5.3, we estimate the carbon abundance within these clouds. The

TABLE 6

TWO-COMPONENT ISM: RESULTS

Ion	Component	b (km s^{-1})	log N (cm^{-2})	log N/H + 12
C II	I	4.0–10.0[a]	14.16 ± 0.41	8.08 (8.56)
	II	3.5–10.0[a]	14.32 ± 0.57	8.08 (8.56)
N I	I	6.4 ± 3.0	13.43 ± 0.08	7.35 (8.05)
	II	6.8 ± 2.5	13.57 ± 0.07	7.33 (8.05)
O I	I	3.3–10.0[a]	14.50 ± 0.44	8.42 (8.93)
	II	2.8–10.0[a]	14.65 ± 0.59	8.41 (8.93)
Si II	I	4.7 ± 0.7	12.76 ± 0.03	6.68 (7.55)
	II	3.2 ± 0.3	13.46 ± 0.08	7.22 (7.55)
Si III......	I	...	...	...
	II	3.0–10.0[a]	12.37 ± 0.13	6.13 (7.55)
S II	I	...	...	...
	II	≥1.0	13.76 ± 0.14	7.52 (7.27)

[a] Assumed range of b-values.

abundances are uncertain but may indicate carbon depletion (-0.48 dex) relative to the cosmic abundance ratio (in parenthesis, Table 6) in the local ISM possibly due to EUV ionizing radiation.

Within cloud II, the ratio of the ground-state and excited-state column densities at $b = 3.5$, 5.0, and 10.0 km s^{-1} is $n_j/n_k = 70.8$, 15.5, and 6.3, respectively. A detailed balancing argument suggests that

$$\frac{\gamma_{kj} n_e + A_{kj}}{n_e \gamma_{jk}} = \frac{n_j}{n_k} ,$$

$$\frac{1.86 \times 10^{-7} n_e + 2.291 \times 10^{-6}}{9.29 \times 10^{-8} n_e} \sim 6.3\text{–}70.8 ,$$

where n_j corresponds to $E = 0$ and n_k to $E = 63.42$ cm^{-1}; A_{kj} is from Galavis, Mendoza, & Zeippen (1998), and γ_{kj} and γ_{jk} are from Blum & Pradhan (1992) who include a more detailed C II atom than Hayes & Nussbaumer (1984). We adopted Blum & Pradhan's collision strength value of $\Omega = 2.15$ ($T_{\rm ISM} = 10^4$ K) versus 2.90 from Hayes & Nussbaumer.

Solving for the electron density, we obtain $n_e = 1.8$–5.7 cm^{-3} for $b = 5.0$–10.0 km s^{-1} and a much lower density $n_e = 0.36$ for the improbably low velocity dispersion $b = 3.5$ km s^{-1}. The density appears much higher than values toward RE J1032+532 (0.11 cm^{-3}) obtained using similar assumptions on the velocity dispersion (Holberg et al. 1999) and toward Capella (Wood & Linsky 1997). Gry et al. (1995) also found $n_e = 0.09$ cm^{-3} toward ϵ CMa. The much higher density measured in ISM component II is hypothetically associated with a circumstellar shell about Feige 24. On the other hand, the low average electron density rules out significant populations of the excited Si II level at 287 cm^{-1} or the O I levels at 158 and 227 cm^{-1}. *Far-Ultraviolet Spectroscopic Explorer* (*FUSE*) measurements of the C II λ1036.8 doublet may help estimate b within component II of this line of sight and reduce the uncertainty on the electron density measurement.

5.5. N I, O I, Si II, *and* S II *Column Densities*

Figure 5 presents a curve-of-growth analysis of the ultraviolet N I triplet using line data from Morton (1991). Lines from both clouds are in the unsaturated part of the curve of growth, and only the column densities are well constrained, and not the velocity dispersions. Table 6 lists measured parameters: N I appears equally depleted (~ -0.7 dex) in both clouds suggesting comparable exposures to EUV ionizing radiation.

A single O I line cannot constrain simultaneously the O I column density and velocity dispersion. Assuming a plausible range for the parameter b, we find possible depletion of oxygen by ~ -0.5 dex in both clouds (Table 6).

Figure 6 shows the same analysis but for the ultraviolet Si II lines with line data from Luo, Pradhan, & Shull (1988).

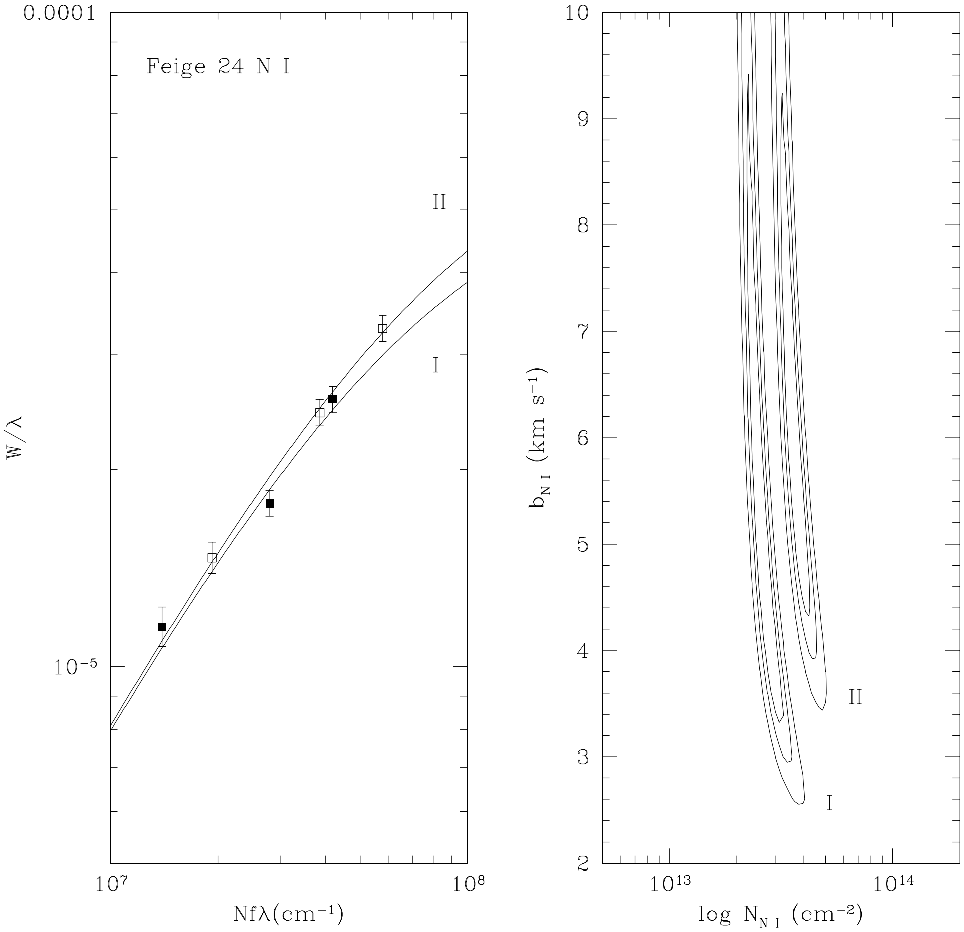

FIG. 5.—Curve-of-growth analysis of the ultraviolet N I triplet in the summed *HST* STIS spectrum (*left panel*) and confidence contours (66%, 90%, and 99%) in the log N vs. b-plane (*right panel*). Two distinct clouds (I and II) are detected.

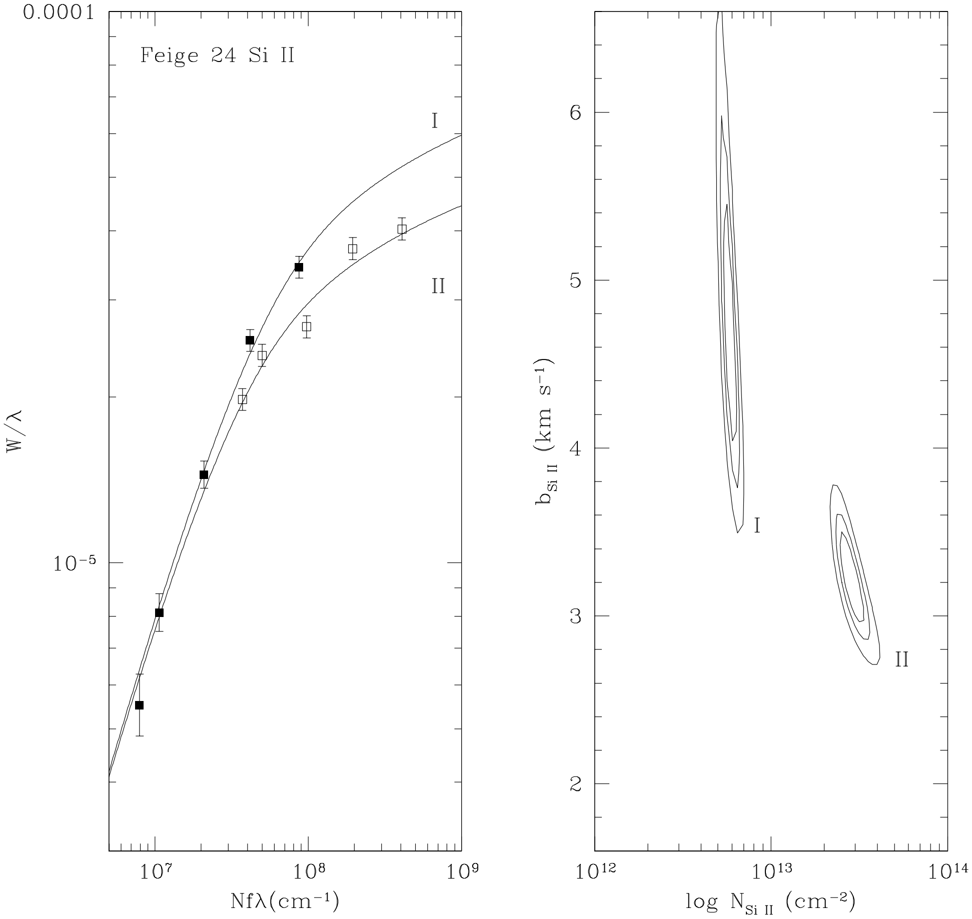

FIG. 6.—Same as Fig. 5 but for the five ultraviolet Si II lines. Two distinct clouds (I and II) are detected.

Silicon appears depleted in both clouds, by ∼ −0.7 dex in cloud I and ∼ −0.3 dex in cloud II (Table 6). Signification variations are noted between clouds I and II indicating the effect of different ionizing radiation fields or grain aggregates. The Si III column density within cloud II constitutes 10% of the combined Si II/Si III column density.

Finally, Figure 7 shows the same analysis but for the ultraviolet S II lines with line data from Morton (1991). Sulfur is detected within cloud II only and is found in proportion slightly larger than the cosmic value.

5.6. C IV *and* Si IV *Column Densities*

The circumstellar C IV equivalent widths based on STIS spectra (Table 7) are only half of previous measurements (Dupree & Raymond 1982; VT94). Excellent signal-to-noise ratio achieved in the present observation and its superior spectral resolution encourage us in adopting the present results. The effect on the column density is only marginal and a curve-of-growth analysis results in log $N_{\rm C\,IV} = 13.46 \pm 0.20$ and $b_{\rm C\,IV} \geq 3.7$ km s^{-1}. The origin of the C IV features is uncertain (see a discussion of ϵ CMa by Gry et al. 1995), but due to its large radial velocity variations Feige 24 is one of a few cases where a "nebular" component can be separated from the photospheric component. The C IV velocity excludes an association with the LIC but instead suggests an association with cloud II or with a circumstellar shell about Feige 24. Our GHRS observation of the DA plus dMe binary EUVE J0720−317 revealed similar

TABLE 7

HIGH-IONIZATION SPECIES IN THE ISM OR CIRCUMSTELLAR ENVIRONMENT

Ion	$\lambda_{\rm lab}$ (Å)	f_{ij}[a]	$\lambda_{\rm obs}$ (Å)	EW (mÅ)	v (km s^{-1})	Analysis
C IV......	1548.195	0.1908	1548.240	65.2	+8.7	Possibly circumstellar
	1550.770	0.0952	1550.807	40.9	+7.2	log $N_{\rm C\,IV} = 13.46 \pm 0.20$, $b \geq 3.7$ km s^{-1}
Si IV......	1393.755	0.5140	1393.785	6.4	+6.5	Possibly circumstellar
	1402.770	0.2553	1402.799	6.1	+6.2	log $N_{\rm Si\,IV} = 11.95 \pm 0.15$, if $b \geq 3$ km s^{-1}

[a] f_{ij} from Morton 1991.

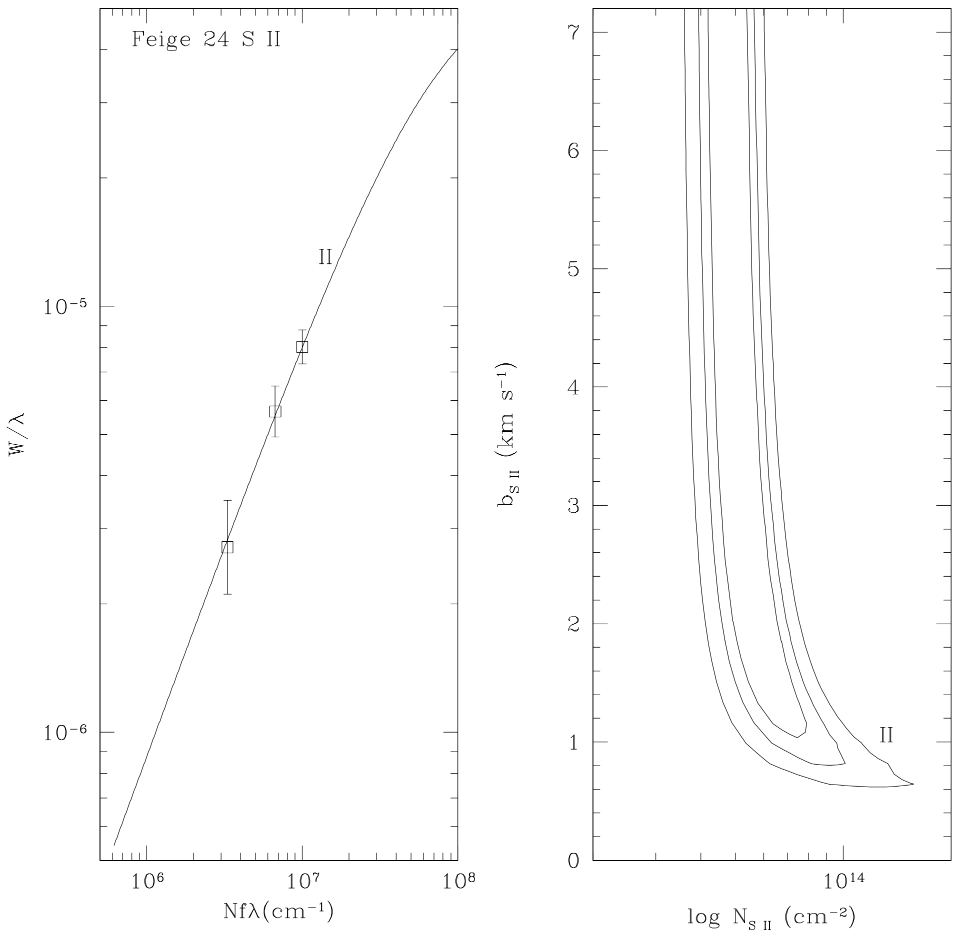

FIG. 7.—Same as Fig. 5 but for the ultraviolet S II triplet. A single cloud (II only) is detected.

"nebular" C IV absorption (Vennes, Thorstensen, & Polomski 1999).

Table 7 also lists weak Si IV absorption at the limit of detection. The Si IV and C IV doublets are at the same velocity and may originate from the same region.

5.7. *Summary of ISM Properties*

We have identified two distinct components in the ISM line absorption, with the component at +17 km s^{-1} possibly associated with the LIC. Column density measurements of the low-ionization species reveal mild depletion for most elements in both clouds (~ −0.3 to −0.7 dex). We also discussed the likely association of the C IV and Si IV lines with cloud II or with a circumstellar structure about Feige 24. The relative population of the C II ground state and the excited state at $E = 63$ cm^{-1} indicates a relatively high electron density in component II. The presence of an ionized circumstellar structure about Feige 24 may be inferred from the C II and C IV line properties.

The average deuterium abundance toward Feige 24 appears typical of the ISM in lines of sight up to 70 pc from the Sun.

Table 8 summarizes the properties of the ISM line of sight toward Feige 24. Hydrogen and deuterium column densities toward Feige 24 were obtained from the ISM Lyα line profile and the component velocities from the average of the low-ionization species comprising 10 spectral lines for component I and 15 lines for component II (Table 5).

TABLE 8

ISM RESULTS

Parameter	Component	Value
$N_{H\,I}$ (10^{18} cm^{-2})......	I (LIC?)	1.20 ± 0.40
	II	1.75 ± 0.50
	Total LOS	3.0 ± 0.3
$N_{D\,I}/N_{H\,I}$...............	Total LOS	$1.3 \pm 0.5 \times 10^{-5}$
v (km s^{-1})............	I (LIC?) ($n = 10$)	+17.6 ± 0.9
	II ($n = 15$)	+3.1 ± 0.9

6. PHOTOSPHERIC ABUNDANCE

Table 9 reports three different sets of abundance measurements, along with spectral ranges or specific spectral lines fitted. Under the label "LTE" we present a series of measurements based on the co-added *IUE* NEWSIPS spectrum and the co-added *HST* STIS spectrum. The LTE synthetic spectra are based on a model atmosphere (Vennes, Thejll, & Pradhan 1995, private communication) which includes the effect of C, N, O, and Fe opacities with fixed abundance (see Table 2). The two sets of measurements agree to within +0.05 ± 0.13 dex. In the following, we

TABLE 9

PHOTOSPHERIC ABUNDANCE (log X/H)

		LTE[a]		NLTE[b]			
ION	SPECTRAL LINES/RANGES	*IUE* (dex)	STIS (dex)	STIS (dex)	$\Delta_{\rm NLTE-LTE}$ (dex)	d log X/dT (dex 10^{-4} K)	d log X/d log g (dex dex^{-1})
C III.......	1174.75–1176.60	...	−7.51	−7.09 ± 0.10	+0.42	+0.56	−0.38
C IV.......	1548.202,1550.774	−6.9	−6.86	−6.88 ± 0.08	−0.02	+0.30	+0.19
N IV	1718.500	−7.0	−6.93	−6.66 ± 0.10	+0.27	+0.19	+0.19
N V	1238.821,1242.804	−5.9	−5.67	−6.99 ± 0.07	−1.32	+0.00	+0.64
O IV	1338.612,1342.99,1343.512	−5.7	−5.94	−5.77 ± 0.07	+0.17	−0.07	+0.50
O V	1371.292	−5.4	−5.45	−6.60 ± 0.05	−1.15	−0.35	+0.60
Si III	1206.510,1206.533	...	−6.00	−6.39 ± 0.10	−0.39	+0.94	−0.56
Si IV	1393.755,1402.770	−5.9	−5.81	−5.94 ± 0.05	−0.13	+0.55	+0.00
S V........	1501.799	−6.6	−6.55	−5.93 ± 0.08	+0.62	+0.35	+0.25
Fe IV......	1567.0–1569.0,1608.0–1610.5	...	−5.84	−5.50 ± 0.07	+0.34	+0.45	−0.23
Fe V	1373.0–1381.0	−5.5	−5.43	−5.19 ± 0.05	+0.24	−0.19	+0.41
Ni IV......	1421.1–1421.5,1534.5–1535.5	...	−6.38	−5.87 ± 0.08	+0.51	+0.50	−0.25
Ni V	1243.5–1245.5,1276.5–1277.5	−6.2	−6.00	−5.76 ± 0.08	+0.24	−0.19	+0.31

[a] Abundances based on an LTE model at ($T_{\rm eff}$, log g) = (56,000 K,7.5).

[b] Abundances based on a model at ($T_{\rm eff}$, log g) = (57,000 K,7.5), and derivatives based on additional models at (55,000 K, 7.5) and (57,000 K, 7.3).

discuss LTE and NLTE measurements based solely on STIS spectroscopy. The narrow photospheric lines show the effect of mild rotation broadening, and we adopted $v \sin i = 7$ km s^{-1} in the abundance analysis; the models are subsequently degraded to the measured resolving power ($R = 36{,}600$). Figure 8 shows the best NLTE model fits based on a model at $T_{\rm eff} = 57{,}000$ K, and log $g = 7.5$.

6.1. *Carbon*

LTE.—Carbon was first identified in *IUE* high-dispersion spectra by Dupree & Raymond (1982). WHS adopted an effective temperature of $T_{\rm eff} = 63{,}000 \pm 10{,}000$ K (log $g = 8$) and estimated a carbon abundance of log C/H = −6.4 ± 0.6 based on the C IV λ1549.1 doublet measured in *IUE* spectra. WHS used synthetic spectra based on a pure hydrogen model structure. An abundance analysis of the C IV doublet based on LTE models which include OP heavy-element cross sections (Table 2, model LTE/OP) yields log C/H = −6.9, in agreement with WHS's result.

NLTE.—Figure 8 shows the best NLTE model fit to the C III λ1175.7 sextuplet and the C IV doublet. The two measurements are in agreement showing that the ionization balance agrees with the adopted atmospheric parameters (effective temperature and surface gravity) and the details of the atomic models. Note that the spectrum near 1175 Å is noisy and that details of the C III sextuplet are not well reproduced. Note also that the LTE/OP and NLTE abundances based on C IV yield similar results.

6.2. *Nitrogen*

LTE.—Nitrogen was also observed in Feige 24 by Dupree & Raymond (1982). WHS derived an abundance of log N/H = −5.3 ± 1.0. The LTE/OP analysis of the N IV λ1718.5 and N V λ1240.1 doublet is inconsistent suggesting the effect of NLTE ionization shifts: the abundance based on the N V line exceeds the abundance based on the N IV line by +1.1 dex.

NLTE.—The NLTE analysis results in a complete reversal of the ionization balance with a residual shift of only log N IV/N V = +0.3. The remaining discrepancy suggests that further adjustments to the atmospheric structure might be required. Minor details of the model atoms, causing the apparent ionization imbalance, may also be incorrect. Nevertheless, the NLTE analysis shows that the LTE/OP models overestimate the nitrogen abundance based on the N V doublet by +1.3 dex.

6.3. *Oxygen*

LTE.—The abundance based on the O V λ1371 line exceeds the abundance based on the O IV λ1341.8 triplet by +0.5 dex.

NLTE.—The O IV/O V ionization balance appears overcorrected by −0.8 dex in the NLTE model. The NLTE and LTE abundance measurements based on O IV agree well and are between log O/H = −5.8 and −5.94, but modeling of the O V λ1371.292 line proves difficult in both contexts.

6.4. *Silicon*

LTE.—Silicon is the third and last photospheric element observed by Dupree & Raymond (1982). WHS measured an abundance of log Si/H = −6.3 ± 0.9, based on the Si IV λ1396.7 doublet. The detection of weak Si III λ1206.510–1206.533 in the STIS spectrum yields an abundance lower than the abundance based on the Si IV doublet. The Si III λ1298.9 sextuplet is only marginally detected and has not been used in the abundance determination.

NLTE.—The abundance measurements based on LTE and NLTE analyses are similar, but the NLTE analysis of the Si III/Si IV ionization balance may require further adjustment to either the model temperature structure or the silicon model atom.

6.5. *Sulfur*

LTE.—A study of the S V λ1501.799 line yields a sulfur abundance (log S/H = −6.6) similar to the sulfur abundance measured in G191-B2B using S IV lines (Vennes et al. 1996). A combination of FUV data from *HST* STIS and a *FUSE* spectrum would permit a detailed analysis of the S IV/S V ionization balance in the atmosphere of Feige 24.

NLTE.—The NLTE analysis yields a sulfur abundance +0.6 dex larger. Clearly, a combined analysis of FUV S IV

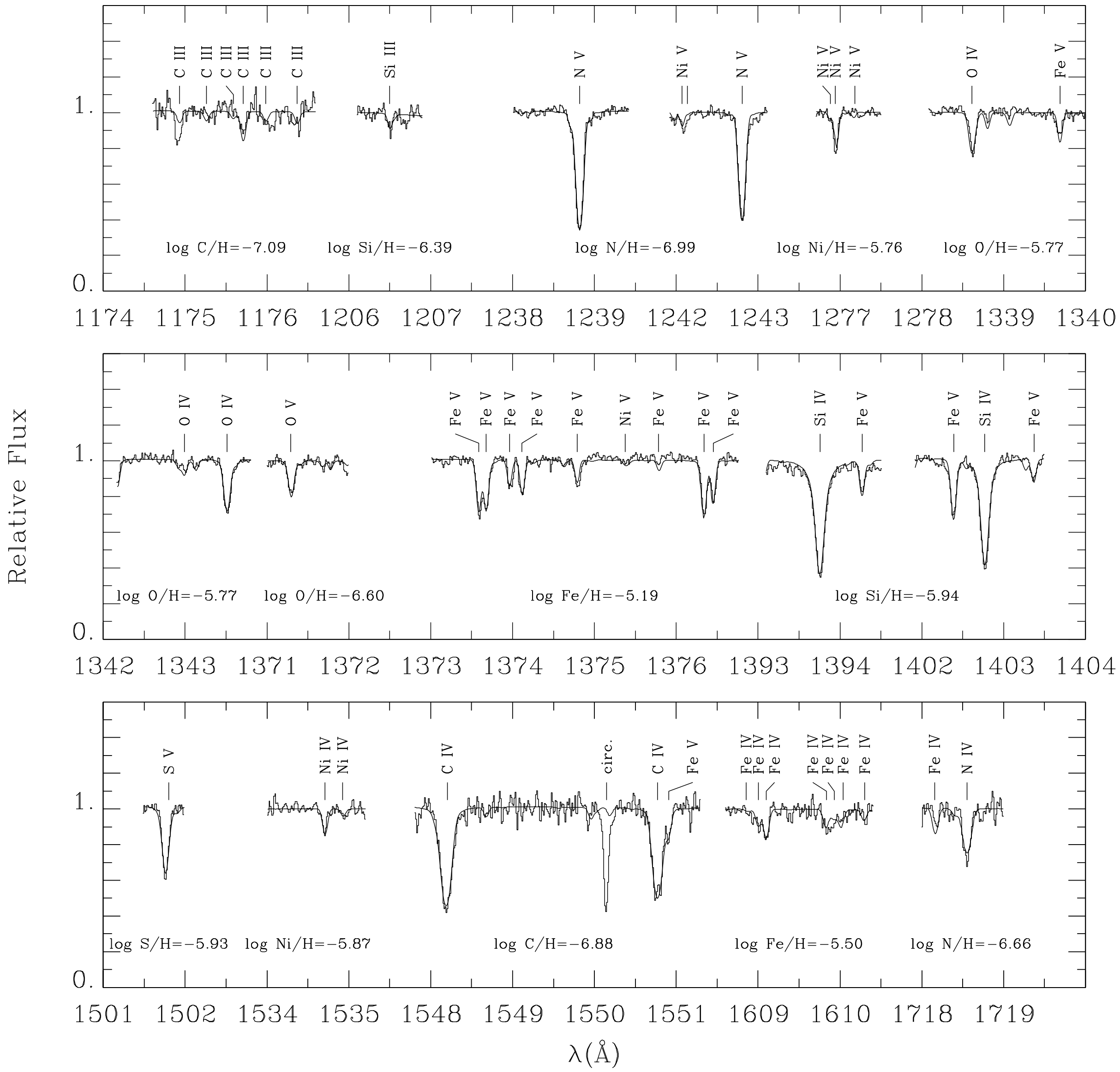

FIG. 8.—Summed *HST* STIS spectra and best NLTE model fit for each ionic species. The NLTE models are described in § 3 and the spectra in § 2.2.

and S V lines may help ascertain details of the model atom in the present calculations.

6.6. *Iron*

LTE.—Several Fe IV lines are detected in the STIS spectra allowing for the first time a detailed study of the iron ionization balance. The present iron abundance measurement based on Fe V is close to the original estimate of Vennes et al. (1992). Virtually all Fe VI lines of interest are blended with strong Ni V lines, and an abundance analysis was not attempted.

NLTE.—The Fe IV/Fe V NLTE ionization balance is close to LTE calculations. On the other hand, NLTE calculations result in a global +0.3 dex abundance increase relative to LTE calculations. Large NLTE ionization effects on the Fe IV/Fe V balance—up to a factor of 100, predicted by Dreizler & Werner (1993), and to a lesser degree up to factor of 10 by Lanz & Hubeny (1995) in NLTE models at $T_{\rm eff} =$ 55,000–60,000 K and $\log g = 7.5$—are not observed in Feige 24. Moreover, these effects are not reproduced in the present generation of calculations. Incompleteness of the first generation of NLTE iron model atoms may be responsible for these unrealistically large ionization effects. Werner & Dreizler's (1994) abundance measurement, based on Fe V lines, is $\log {\rm Fe/H} = -5.0 \pm 0.1$ and is close to the present measurement.

6.7. *Nickel*

LTE.—As for most elements, the detection of two nickel ionization states permits a study of the ionization balance, and a study of LTE abundances based on Ni IV and Ni V lines results in an ionization imbalance of +0.4 dex.

NLTE.—The apparent imbalance in LTE is, within measurement errors, corrected in the present NLTE calculations. The resulting nickel abundance is 0.4 dex larger than the LTE value. Werner & Dreizler's (1994) abundance measurement based on Ni V lines is $\log {\rm Ni/H} = -5.65 \pm 0.35$, close to the present measurement.

6.8. *Derivatives of Abundance with Temperature and Gravity*

We have found that the oxygen abundance is still uncertain due to an inconsistent O IV/O V ionization balance.

Adjustment of the effective temperature and surface gravity may, at least in part, correct the situation. The ionization balance of other elements also appears, to a lesser extent, incorrect while a few, C III/C IV in particular, are well reproduced. It is important to determine how variations of stellar parameters, in particular, the effective temperature, may affect the ionization imbalance problem and how details of the model atoms may also affect the problem.

Table 9 presents the effects small variations in temperature and surface gravity around 57,000 K and $\log g = 7.5$ would have on abundance measurements. Using models with 2000 K temperature or 0.2 dex gravity increments, we calculated the derivatives of the abundance with respect to effective temperature ($d \log \mathrm{X}/dT$) and with respect to gravity ($d \log \mathrm{X}/d \log g$). The derivatives are valid for small increments and indicate trends only. The ionization balance of carbon, silicon, and iron would be improved by increasing the effective temperature, but the ionization balance of nitrogen and oxygen would be worsened. The ionization balance of carbon, silicon, iron, and nickel would also become inconsistent with an increase in surface gravity, but all derivatives with respect to surface gravity show that only small corrections on the abundance (≤ 0.2 dex) would be obtained by a likely shift in surface gravity of 0.2 dex or less. We conclude that residual ionization imbalances of some elements are rooted in the details of the model atoms required for the NLTE calculations.

7. SUMMARY

Our revised estimates of the white dwarf mass and radius reflect a proposed ~ 9 km s^{-1} correction to the stellar and ISM velocity scales obtained with STIS relative to the *IUE* high-dispersion velocity scale. Assuming that the STIS velocity scale is indeed correct, we may associate one of the two ISM velocity components with the LIC (component I). Noting that the *IUE* velocity scale is internally consistent, we conclude that all *IUE* velocity measurements of Feige 24 are systematically low by ~ 9 km s^{-1}. Still assuming that the STIS velocity scale is correct, we find a good agreement between the *HST* FGS 3 parallax measurement and our new gravitational redshift. Unfortunately, the white dwarf surface gravity measurements are still between 0.1 and 0.4 dex smaller than predicted by the updated mass and radius estimates. Measurements of the FUV Lyman line series with *FUSE* may help constrain the surface gravity.

The association of cloud I with the LIC is supported by column density measurements of C II, N I, O I, and Si II ISM lines which, when divided by the respective H I column densities within clouds I and II, reveal plausible cosmic abundances in both clouds. Our high-dispersion study does reveal a connection between some of the gas in the line of sight toward Feige 24 and the LISM. Analysis of the deuterium-to-hydrogen abundance ratio supports a relative constancy of this ratio throughout the local ISM up to a distance of 70 pc.

We have presented the first complete abundance pattern in the white dwarf showing predominance of oxygen, iron, and nickel over other elements. Problems with ionization balance, notably for oxygen, remain and need to be resolved before more sophisticated interpretations of EUV and FUV spectral properties are offered (see Dreizler & Wolff 1999). However, as a much better match of the O IV and O V lines is achieved for hot subdwarfs with similar NLTE model atmospheres (Lanz et al. 1997; Hubeny et al. 1999), we suggest that the measured ionization imbalance in Feige 24 might reveal an inhomogeneous vertical stratification of oxygen in the white dwarf photosphere. Considering its relatively high abundance in Feige 24's atmosphere, actual opacity calculations for nickel, as opposed to an application of hydrogenic calculations, should also be included. With respect to LTE, the NLTE calculations reconcile the abundances derived from C III and C IV lines and from N IV and N V lines. They yield higher abundances for sulfur, iron, and nickel, by 0.3–0.6 dex. We found that Fe IV is present in the photosphere of Feige 24 showing the usefulness of detailed data analysis in ascertaining NLTE model calculations.

A comparison with the hot DA white dwarf G191-B2B is instructive. The two stars share similar atmospheric parameters and almost identical abundance pattern. Table 10 compares the adopted abundances in Feige 24, taken as the straight average of NLTE/STIS measurements from Table 9, and the abundances in G191-B2B from Lanz et al. (1996). Lanz et al. used *IUE* spectra and a generation of NLTE models comparable to the present generation of models. The abundances are remarkably similar, *except for carbon* which appears underabundant in Feige 24 relative to G191-B2B by ~ 1.4 dex. The discrepancy may be due to the presence of circumstellar or interstellar contamination of the C IV doublet in G191-B2B which went unaccounted for in the abundance measurements. The similarity of all other abundance measurements indicates that their abundance pattern is determined by processes operating equally in both stars. Such processes may depend solely on stellar parameters such as T_{eff} and $\log g$. Atmospheric diffusion in the presence of selective radiation pressure, mass loss, or alternatively accretion remain key processes in determining abundance in white dwarf stars (Chayer et al. 1994, 1995). However, carbon, nitrogen, oxygen, and nickel appear underabundant relative to diffusion calculations by -1 dex, while iron is closer to the predicted abundance. Silicon exceeds the prediction by $+1$ dex. This curious phenomenon also observed in the case of G191-B2B prompted a suggestion that, perhaps, silicon is accreted in the form of grains (Vennes et al. 1996). The likely explanation for the relative underabundance of some elements remains the presence of a weak mass loss in young white dwarf stars.

TABLE 10

Adopted Abundances in Feige 24 and G191-B2B

Element	Feige 24[a]	G191-B2B[b]
C.........	−6.99	−5.7
N	−6.83	−6.8
O	−6.19	−6.0
Si	−6.16	−6.5
Fe........	−5.35	−5.0
Ni........	−5.82	−5.7

[a] From the present study.

[b] From Lanz et al. 1996.

S. V. is a QE II fellow of the Australian Research Council. We are grateful to the Space Science Telescope Institute and then director R. Williams for rescheduling failed GHRS observations with STIS. This work was supported by NASA grant NAG 5-2636 to the University of California at Berkeley, where the project was initiated.

REFERENCES

Barstow, M. A., Hubeny, I., & Holberg, J. B. 1998, MNRAS, 299, 520

Benedict, G. F., et al. 2000, AJ, 119, 2382

Bluhm, H., Marggraf, O., de Boer, K. S., Richter, P., & Heber, U. 1999, A&A, 352, 287

Blum, R. D., & Pradhan, A. K. 1992, ApJS, 80, 425

Bowyer, S., Lampton, M., Lewis, J., Wu, X., Jelinsky, P., & Malina, R. F. 1996, ApJS, 102, 129

Chayer, P., LeBlanc, F., Fontaine, G., Wesemael, F., Michaud, G., & Vennes, S. 1994, ApJ, 436, L161

Chayer, P., Vennes, S., Pradhan, A. K., Thejll, P., Beauchamp, A., Fontaine, G., & Wesemael, F. 1995, ApJ, 454, 429

Crutcher, R. M. 1982, ApJ, 254, 82

Dreizler, S., & Werner, K. 1993, A&A, 278, 199

Dreizler, S., & Wolff, B. 1999, A&A, 348, 189

Dupree, A. K., & Raymond, J. C. 1982, ApJ, 263, L63

Dupuis, J., Vennes, S., Bowyer, S., Pradhan, A. K., & Thejll, P. 1995, ApJ, 455, 574

Eggen, O. J., & Greenstein, J. L. 1965, ApJ, 141, 83

Feige, J. 1958, ApJ, 128, 267

Finley, D., Koester, D., & Basri, G. 1997, ApJ, 488, 375

Galavis, M. E., Mendoza, C., & Zeippen, C. J. 1998, A&AS, 131, 499

Greenstein, J. L., & Eggen, O. J. 1966, Vistas Astron., 8, 63

Gry, C., Lemonon, L., Vidal-Madjar, A., Lemoine, M., & Ferlet, R. 1995, A&A, 302, 497

Haro, G., & Luyten, W. J. 1962, Bol. Obs. Tonantzintla Tacubaya, 3, 37

Hayes, M. A., & Nussbaumer, H. 1984, A&A, 134, 193

Hébrard, G., Mallouris, C., Ferlet, R., Koester, D., Lemoine, M., Vidal-Madjar, A., & York, D. 1999, A&A, 350, 643

Holberg, J. B., Barstow, M. A., & Sion, E. M. 1998, ApJS, 119, 207

Holberg, J. B., Bruhweiler, F. C., Barstow, M. A., & Dobbie, P. D. 1999, ApJ, 517, 841

Holberg, J. B., Wesemael, F., & Basile, J. 1986, ApJ, 306, 629

Holm, A. V. 1976, ApJ, 210, L87

Hubeny, I. 1988, Comput. Phys. Commun., 52, 103

Hubeny, I., & Lanz, T. 1995, ApJ, 439, 875

Hubeny, I., Lanz, T., Haas, S., Heap, S. R., Lindler, D. J., & Kaiser, M.-B. 1999, BAAS, 31, 930

Lallement, R., Ferlet, R., Lagrange, A. M., Lemoine, M., & Vidal-Madjar, A. 1995, A&A, 304, 461

Lanz, T., Barstow, M. A., Hubeny, I., & Holberg, J. B. 1996, ApJ, 473, 1089

Lanz, T., & Hubeny, I. 1995, ApJ, 439, 905

Lanz, T., Hubeny, I., & Heap, S. R. 1997, ApJ, 485, 843

Liebert, J., & Margon, B. 1977, ApJ, 216, 18

Linsky, J. L., Diplas, A., Wood, B. E., Brown, A., Ayres, T. R., & Savage, B. D. 1995, ApJ, 451, 335

Linsky, J. L., & Wood, B. E. 1998, in ASP Conf. Ser. 143, The Scientific Impact of the GHRS, ed. J. C. Brandt, T. B. Ake III, & C. C. Petersen (San Francisco: ASP), 197

Luo, P., Pradhan, A. K., & Shull, J. M. 1988, ApJ, 335, 498

Margon, B., Lampton, M., Bowyer, S., Stern, R., & Paresce, F. 1976, ApJ, 210, L79

Marsh, M. C., et al. 1997, MNRAS, 286, 369

Morton, D. C. 1991, ApJS, 77, 119

Napiwotzki, R., Green, P. J., & Saffer, R. A. 1999, ApJ, 517, 399

Oke, J. B. 1974, ApJS, 27, 21

Paerels, F. B. S., Bleeker, J. A. M., Brinkman, A. C., & Heise, J. 1986, ApJ, 309, L33

Pradhan, A. K. 1996, in Astrophysics in the Extreme Ultraviolet, ed. S. Bowyer & R. F. Malina (Dordrecht: Kluwer), 569

Pye, J. P., et al. 1995, MNRAS, 274, 1165

Sahu, M. S., et al. 1999, ApJ, 523, L159

Shipman, H. L. 1972, ApJ, 177, 723

Thompson, R. W., Turnrose, B. E., & Bohlin, R. C. 1982, A&A, 107, 11

Thorstensen, J. R., Charles, P. A., Margon, B., & Bowyer, S. 1978, ApJ, 223, 260

Vennes, S., Chayer, P., Fontaine, G., & Wesemael, F. 1989, ApJ, 336, L25

Vennes, S., Chayer, P., Hurwitz, M., & Bowyer, S. 1996, ApJ, 468, 898

Vennes, S., Chayer, P., Thorstensen, J. R., Bowyer, S., & Shipman, H. L. 1992, ApJ, 392, L27

Vennes, S., Thejll, P., Génova-Galvan, R., & Dupuis, J. 1997, ApJ, 480, 714

Vennes, S., & Thorstensen, J. R. 1994, AJ, 108, 1881 (VT94)

Vennes, S., Thorstensen, J. R., & Polomski, E. F. 1999, ApJ, 523, 386

Vennes, S., Thorstensen, J. R., Thejll, P., & Shipman, H. L. 1991, ApJ, 372, L37

Werner, K., & Dreizler, S. 1994, A&A, 286, L31

Wesemael, F., Henry, R. B. C., & Shipman, H. L. 1984, ApJ, 287, 868 (WHS)

Wolff, B., Koester, D., Dreizler, S., & Haas, S. 1998, A&A, 329, 1045

Wood, B. E., & Linsky, J. L. 1997, ApJ, 474, L39

Wood, M. A. 1995, in White Dwarfs, ed. D. Koester & K. Werner (Berlin: Springer), 41